JM PAPERS

Liquid inertia versus bubble cloud buoyancy in circular plunging jet experiments

Narendra Dev[1], **J. John Soundar Jerome**[1], **Hélène Scolan**[1] and **Jean-Philippe Matas**[1,†]

[1]Univ Lyon, Univ Claude Bernard Lyon 1, CNRS, Ecole Centrale de Lyon, INSA Lyon, LMFA, UMR5509, 69622 Villeurbanne, France

When a liquid jet plunges into a pool, it can generate a bubble-laden jet flow underneath the surface. This common and simple phenomenon is investigated experimentally for circular jets to illustrate and quantify the role played by the net gas/liquid void fraction on the maximum bubble penetration depth. It is first shown that an increase in either the impact diameter or the jet fall height to diameter ratio at constant impact momentum leads to a reduction in the bubble cloud size. By measuring systematically the local void fraction using optical probes in the biphasic jet, it is then demonstrated that this effect is a direct consequence of the increase in air content within the cloud. A simple momentum balance model, including only inertia and the buoyancy force, is shown to predict the bubble cloud depth without any fitting parameters. Finally, a Froude number based on the bubble terminal velocity, the cloud depth and also the net void fraction is introduced to propose a simple criterion for the threshold between the inertia-dominated and buoyancy-dominated regimes.

Key words: bubble dynamics, gas/liquid flow

1. Introduction

The impact of a plunging jet on the free surface of a pool of the same or a different liquid above a critical velocity transports ambient gas into the continuous liquid phase, thus forming a cluster of bubbles, a bubble cloud (Lin & Donnelly 1966; Bonetto, Drew & Lahey 1994; Zhu, Oğuz & Prosperetti 2000; Lorenceau, Quéré & Eggers 2004). This phenomenon is encountered widely in industrial applications, such as the stirring of chemicals (McKeogh & Ervine 1981) or hydroelectric applications (Guyot 2019), and in nature, as in breaking waves and cascades (Chanson 2002; Kiger & Duncan 2012).

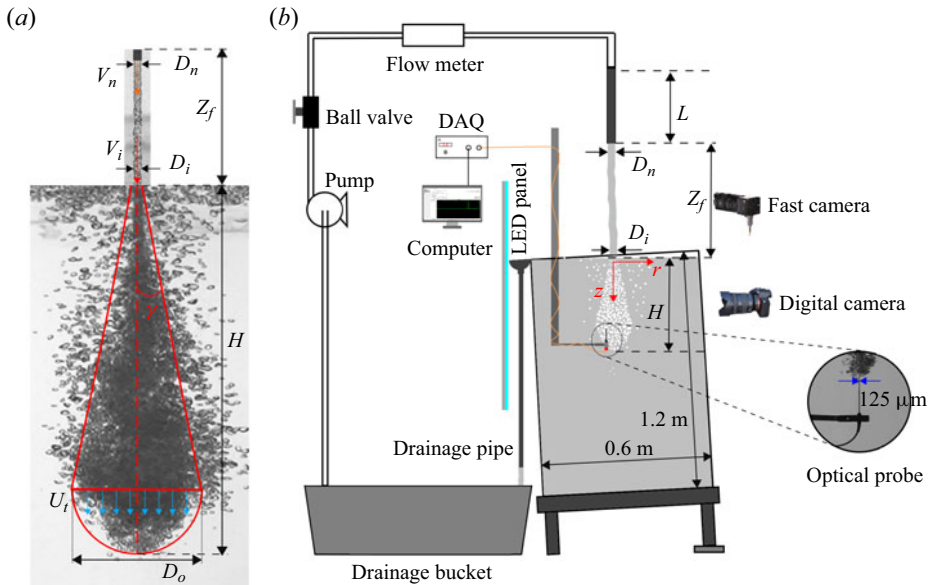† Email address for correspondence: jean-philippe.matas@univ-lyon1.fr

Figure 1. (*a*) Schematic of the control volume of the bubble cloud. (*b*) Schematic of the experimental set-up, illustrating flow lines to generate the bubble cloud, the backlighting imaging set-up and the void fraction measurement set-up with optical probes.

Previous studies discussed the inception of air bubbles below jet impact and proposed models for the air entrainment mechanism based on the morphology in circular (McKeogh & Ervine 1981; Sene 1988; El Hammoumi, Achard & Davoust 2002) and planar (Cummings & Chanson 1999; Bertola, Wang & Chanson 2018) jets, as well as multi-droplet streams (Speirs *et al.* 2018). Kiger & Duncan (2012) reviewed the air entrainment mechanism for laminar, turbulent and disintegrated jets of different viscosities. Once the bubble entrainment conditions are reached, the maximum penetration depth of the bubble cloud, denoted by H in figure 1(*a*), is an essential parameter to model in various applications (Clanet & Lasheras 1997). Indeed, a change in H will affect the volume of the biphasic region and alter the gas mixing rate in chemical industries. In hydroelectric power plants, H is critical in designing dams to prevent erosion and structural weakening caused by the incoming biphasic jet hitting the river bed. As can be inferred from table 1, previous studies have addressed bubble cloud formation over a wide range of scales (Biń 1993; Clanet & Lasheras 1997; Chirichella *et al.* 2002; Roy, Maiti & Das 2013; Qu *et al.* 2013; Harby, Chiva & Muñoz-Cobo 2014; Kramer, Wieprecht & Terheiden 2016; Miwa *et al.* 2018; Guyot, Cartellier & Matas 2020). Evidence for strong scale effects exists not only regarding bubble cloud size but also for bubble count rate or void fraction (Chanson, Aoki & Hoque 2004). Whereas numerous empirical correlations for the cloud depth can be found in the literature depending on their size, from a few centimetres to about a few metres, the underlying physics has been elaborated only recently.

In this context, Clanet & Lasheras (1997) developed a jet momentum conservation argument, similar to the work of Suciu & Smigelschi (1976), but by postulating that (i) the biphasic jet expands with a constant cone half-angle $\gamma = 12.5°$, as is well known in turbulent jets (Horn & Thring 1956; Ervine & Falvey 1987; L'vov *et al.* 2008), and (ii) bubbles would escape the biphasic zone as soon as the local advection speed, due to the

Author(s) (year)	Jet and nozzle geometry	D_n (mm)	V_n (m s^{-1})	Z_f (cm)	$Re = \rho V_n D_n/\mu$ (max)
Lin & Donnelly (1966)	↓ ◯	2–8	0.8–2	1–17	2.5×10^3
Van de Sande & Smith (1973, 1976)	╱ ◯	2.85–10	3–25	10–40	1.12×10^5
van de Donk (1981)	↓ ◯	4–30	4–10	20–85	2.8×10^5
McKeogh & Ervine (1981)	╱ ↓ ◯	6–30	1–7	50–500	1.1×10^5
Clanet & Lasheras (1997)	↓ ◯	0.24–2.16	1.9–18	0.7–4	1.4×10^4
Cummings & Chanson (1999)	↓ ▢	3–10	1.1–2	0.5–18	1.16×10^4
Chanson & Manasseh (2003)	↓ ◯	14–25	0.5–5	5–20	1.6×10^5
Chanson et al. (2004)	↓ ◯	6.8–25	1.7–4.4	3–10	1.23×10^5
Harby et al. (2014)	↓ ◯	4–14	2.5–13	2.5–30	9×10^4
Kramer et al. (2016)	↓ ◯	13–81.9	5–7	20–100	6.4×10^5
Bertola et al. (2018)	↓ ▢	10.4–11.5	2.4–7.4	10.4–12.7	9.4×10^4
Guyot, Cartellier & Matas (2019)	⇄ ◯	0.3–2.4	1.89–20	0.6–4.8	2.4×10^4
Guyot et al. (2020)	↓ ◯	0.3–213	3–28	20–950	3×10^6
Present study	↓ ◯	2.7–10	2.5–10	5–80	1×10^5

Table 1. Flow conditions in previous works on vertical (↓), inclined (╱) and oscillating (⇄) plunging jets from circular (◯) and planar (▢) nozzles. All authors used water. Data in Lin & Donnelly (1966) refer also to oil and glycol jets.

liquid jet below the free surface, decreases down to the terminal velocity U_t. They thereby derive a simple prediction for the bubble cloud depth H_i:

$$H_i = \frac{1}{2 \tan \gamma} \left(\frac{V_i D_i}{U_t} \right), \tag{1.1}$$

where V_i is the impact velocity and D_i is the impact diameter. Note that there is no adjustable parameter nor any liquid or gas physical properties in (1.1), except for U_t, which is taken equal to 22 cm s^{-1} for all air bubbles in water larger than 1 mm in diameter (Maxworthy et al. 1996). Equation (1.1) shows that in this case, the cloud depth is directly proportional to $V_i D_i$, which, up to a factor of liquid density ρ, is the square root of the impact momentum. Clanet & Lasheras (1997) obtained very good agreement for their experiments with micro-jets, of at most 2.16 mm in nozzle diameter. However, unlike single-phase jets in a neutrally buoyant environment, momentum conservation may not be valid for voluminous biphasic jets, for which buoyancy cannot be neglected. For example, in a 15 cm deep conical bubble cloud that contains only a small void fraction of air, say $\phi = 10\%$, the outgoing momentum $\dot{Q}_o \sim (1 - \phi)\rho U_t{}^2 \pi H^2 \tan^2 \gamma$ in figure 1(a) is already comparable to the net buoyancy force $F_b \sim \phi \rho g \pi H^3 \tan^2 \gamma/3$ acting on it. Indeed, the largest cloud in experiments by Clanet & Lasheras (1997) is about 16 cm deep, and (1.1) overpredicts the cloud depth data in the previous literature (Biń 1993; see figure 29 and references within) for much deeper clouds.

More recently, Guyot et al. (2020) extended the above momentum balance model by accounting for buoyancy effects under the assumption that the void fraction within the bubble cloud was uniform. They applied the momentum balance across the truncated conical control volume in figure 1(a) to obtain the following equation for the modelled

cloud depth H_b:

$$\underbrace{\rho V_i V_n \frac{\pi D_n^2}{4}}_{\text{Incoming momentum flux}} = \underbrace{\left(1 - \bar{\phi}\right) \rho U_t^2 \pi \left(H_b \tan \gamma + \frac{D_i}{2}\right)^2}_{\text{Outgoing momentum flux}}$$

$$+ \underbrace{\bar{\phi}\rho g\pi \left(\frac{1}{3} H_b^3 \tan^2 \gamma + \frac{D_i}{2} H_b^2 \tan \gamma + \frac{D_i^2}{4} H_b\right)}_{\text{Buoyancy force}}, \qquad (1.2)$$

where D_n is the nozzle diameter, V_n is the velocity at the nozzle and $\bar{\phi}$ is the constant void fraction. Note that the impact void fraction and diameter have been removed from the impact momentum term on the left-hand side using mass conservation, $V_n D_n^2 = (1 - \bar{\phi})V_i D_i^2$. For the limiting case of micro-jets and bubble cloud depths of 10 cm or less, the buoyancy force may become less important than the outgoing momentum flux in (1.2), which then reduces to (1.1). Conversely, in the limit of very large jets, or massive bubble clouds ($H > 20$ cm), the contribution of the outgoing momentum flux becomes negligible, and (1.2) reduces to the impact momentum being consumed entirely by buoyancy. The fact that a contribution proportional to a surface term is balanced by a contribution proportional to a volume term then leads to H being proportional to $(V_i V_n)^{1/3} D_n^{2/3}$. This is close to the empirical correlation $H \propto (V_n D_n)^{0.66}$ proposed by van de Donk (1981) and $H \propto (V_n D_n)^{0.7}$ proposed by McKeogh & Ervine (1981). Hence, based on physical arguments, (1.2) elucidates the two most common empirical relations, namely, $H \propto V_n D_n$ and $H \propto (V_n D_n)^{0.66}$, over a very wide range of jet diameters and all available data in the current literature (Biń 1993; Guyot *et al.* 2020).

Furthermore, all parameters in the cubic polynomial for H_b are known *a priori*, except for the average gas/liquid void fraction $\bar{\phi}$. So Guyot *et al.* (2020) adopted $\bar{\phi} = 15\%$ based on results from past studies (van de Donk 1981; McKeogh & Ervine 1981) and obtained a relatively good agreement with large-scale experiments. However, they observed a significant dispersion for the cloud depth in both their data and previous investigations when the jet diameter is large. Guyot *et al.* (2020) attributed this dispersion to variations in the void fraction $\bar{\phi}$ between various experiments since it is expected to depend strongly on both the jet geometry and the dynamics (McKeogh & Ervine 1981; Sene 1988; Bonetto *et al.* 1994; Zhu *et al.* 2000). Therefore, even if the scaling law for the bubble cloud depth is understood to some extent, measurements of the actual values of the void fraction ϕ are needed to clarify the role of this quantity in producing the observed dispersion in the cloud depth data. The conditions for the transition from jet-momentum-dominated to buoyancy-dominated clouds remain to be established as well. In addition, such investigations can provide insights into how, when and where additional features of the bubble cloud – such as turbulent dissipation, bubble size distribution and bubble cloud shape – are necessary for dimensioning industrial applications.

Biń (1993) lists correlations based on both global gas/liquid entrainment ratio measurements, using gas holdup techniques, and local gas/liquid void fraction measurements, often using resistivity probes within a bubble cloud. More recent developments on various correlations, along with inception conditions and some mechanistic viewpoints on air entrainment rate, can be found in Kiger & Duncan (2012). Past studies evidence that in the developing region, ϕ radial profiles consist of two maxima located at the radius of the free jet and a minimum at the jet axis (van de Donk 1981;

Bonetto & Lahey 1993; Cummings & Chanson 1997; Brattberg & Chanson 1998; Chanson & Manasseh 2003; Ma *et al.* 2010). McKeogh & Ervine (1981) and van de Donk (1981) measured ϕ in the fully developed region and reported that the peak void fraction ϕ_0 occurs along the cloud axis, remains almost constant with depth and then sharply decreases. However, the current literature lacks measurements of the cloud depth H along with measurements of the local void fraction ϕ in the developed zone of the plume. Such data over various values of the impact momentum and jet fall height are necessary for better understanding of the dynamics of bubble clouds in the buoyancy-dominated regime.

To address this gap, the objective of the present work is to report concurrent local void fraction (ϕ) and bubble cloud depth (H) measurements, for three typical nozzle diameters and at several impact momentum values and fall heights Z_f. Thereby, our aim is twofold: we examine not only the robustness and the relevance of the momentum balance models (Suciu & Smigelschi 1976; Clanet & Lasheras 1997; Guyot *et al.* 2020) by incorporating *in situ* void fraction data into (1.2), but also the effect of the void fraction on the maximum penetration depth of a two-phase plume, by varying independently three major parameters, namely, nozzle diameter, impact momentum and fall height. Using such a case study, we also try to propose a simple criterion to determine when the bubble cloud size is controlled by inertia and when it is controlled by buoyancy.

2. Methodology

Lab-scale experiments are carried out using a 1.2 m × 0.6 m × 0.6 m glass tank that is slightly tilted on one side so that overflowing water is drained through a drainage pipe to the reservoir bucket to keep the water level constant, as shown in figure 1(*b*). Pumps supply water from the drainage bucket to the straight injector, from which it is issued as a plunging jet. Three nozzle diameters D_n are used: $D_n = 2.7$, 8 and 10 mm. For nozzle diameter $D_n = 2.7$ mm, a series of two centrifugal pumps from Pan World (NH-100PX and NH-200PS) is used. A heavy-duty centrifugal pump (2KVC AD 45/80M) from DAB Pumps generates the jet from the larger 8 mm and 10 mm injectors. The injector length to diameter ratio (L/D_n) is kept equal to 50, and the height of fall to diameter ratio Z_f/D_n is varied from 20 up to 100. The nozzle velocity V_n varies from 1.5 to 12 m s^{-1} and is controlled using a flow meter and ball valve. The impact velocity V_i is deduced using the equation $V_i = \sqrt{V_n^2 + 2gZ_f}$. The present work considers only cases where the jet is not broken into droplets before impact.

Backlight imaging is used to film the jet just before the impact, illuminated by an LED panel, using a CMOS fast camera from Ximea (CB262MG) at 300 fps and 20 µs shutter speed at 2496 × 2418 resolution. Images of the biphasic bubble cloud are filmed using a digital camera (Sony a7 III) and a zoom lens (Sony FE 24–70 mm F/4 ZA OSS Carl Zeiss, with focal length kept at 35 mm) at 50 fps and 200 µs exposure at resolution 1920 × 1080 pixels. Using a MATLAB-integrated calibration application, lens distortion was found to be negligible, and constant spatial resolutions 54 and 333 µm pixel^{-1} were used for jet and bubble cloud images, respectively. The cloud images are analysed using the open-source freeware *ImageJ* (Schindelin *et al.* 2012) and algorithms therein for brightness thresholding (Kapur, Sahoo & Wong 1985; Tsai 1985), along with in-house MATLAB code to detect and trace the outer boundaries of the cloud in order to measure H. The mean penetration depth H is measured by averaging over 3000 images. A low frame rate was chosen in order to ensure that the images of the bubble cloud are decorrelated and so that the ensemble average value of the cloud depth H converges faster for a given number of images.

The contours of the jet are extracted from images using machine-learning-based object detection models, namely, grounding DINO (Liu *et al.* 2023) and the Segment Anything model (Kirillov *et al.* 2023). The detected jet edges are then analysed using in-house MATLAB code to obtain the impact diameter (D_i) and the roughness (ϵ). The latter is defined as the average of the root mean square values of the lateral departure from the mean edge position, for each side, and is obtained by averaging over 200 images.

The local void fraction ϕ is measured using an optical fibre probe (A2 Photonics Sensors) of diameter 125 μm mounted upright on a slender plate (thickness 4 mm), as shown in the magnified view in figure 1(*b*). This horizontal plate is fixed to a vertical cylindrical rod (diameter 1.5 cm). The probe tip is located 4.5 cm upstream of this arm. This ensures that obstruction to the incoming flow is minimized as much as possible at the probe tip, where the measurement is carried out. The probe assembly is translated in the vertical (r–z) plane using two motorized linear stages (Igus) having accuracy 0.01 mm. The probe signals are sampled at 250 kHz for 60 s, a duration that is enough to ensure convergence of the void fraction for all conditions. The signals are analysed using A2 Photonics software (SO6 v4.7). The probe is centred at the jet axis, and the measurements are carried out in the radial direction of the cloud with step size 2 mm to obtain radial void fraction profiles. This was repeated at various depths, such that $z/H = 0.4$, 0.6 and 0.8. Note that when the bubble cloud size is measured, the probe assembly is pulled out of the tank with the help of the translation stage.

3. Results and discussion

3.1. *Measurement of bubble cloud depth H*

Figure 2 illustrates the variation of H for the $D_n = 2.7$ mm and $D_n = 8$ mm nozzles, as a function of $\sqrt{V_i V_n} D_n$, which is proportional to the square root of the impact momentum flux, up to a factor of ρ, as in (1.2). Note that the largest bubble cloud obtained for our conditions is 45 cm deep, which is significantly smaller than the tank depth (1.25 m). We therefore assume that there is no significant pressure gradient caused by confinement effects in our experiments. The bubble cloud size H for jets issued from the $D_n = 2.7$ mm nozzle (red and black discs) varies linearly with $\sqrt{V_i V_n} D_n$. This is consistent with the model proposed by Clanet & Lasheras (1997) (solid line; see (1.1)), since for this small-scale jet and for the experimental range considered here, $V_i \approx V_n$ and $D_i \approx D_n$. When Z_f/D_n is increased for this $D_n = 2.7$ mm nozzle, a negligible change in H is observed. For the larger $D_n = 8$ mm nozzle (open symbols), (1.1) predicts accurately the behaviour of H up to $\sqrt{V_i V_n} D_n \approx 0.02$ m^2 s^{-1}. Beyond this threshold, a transition occurs, and H scales as $(V_i V_n)^{1/3} D_n^{2/3}$, in accordance with the model of Guyot *et al.* (2020) (2/3 power law shown by dashed line). This suggests that beyond a threshold, the buoyancy force becomes dominant over the outgoing momentum flux, leading to a decrease in cloud depth H compared with what (1.1) would predict. Also, figure 2 shows the coexistence of two regimes in a narrow range, $\sqrt{V_i V_n} D_n = 0.02$–0.03 m^2 s^{-1}, wherein the inertia-dominated regime occurs for $D_n = 2.7$ mm while buoyancy forces become important for the bigger nozzle diameter. This is perhaps a signature of the dependence of the transition threshold on the void fraction at different jet diameters. Finally, in the buoyancy-dominated zone for $D_n = 8$ mm, some dispersion in the values of H is observed when Z_f/D_n is varied. As mentioned in the Introduction, this dispersion arises from the variations in the net air/water void fraction, as will be discussed in the next subsection.
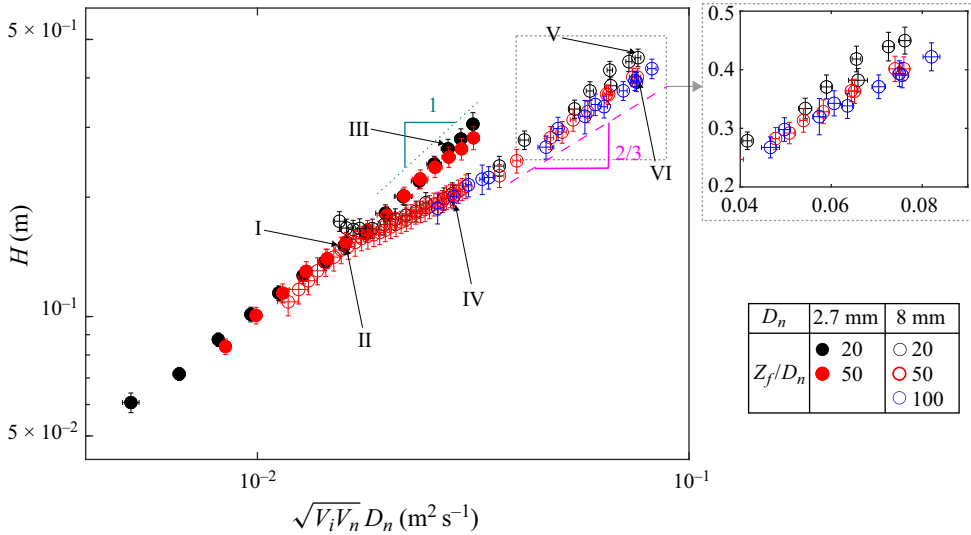
Figure 2. Variation of H with the square root of the impact momentum $\sqrt{V_i V_n}\, D_n$ for $D_n = 2.7$ and 8 mm at various Z_f/D_n. The dotted line shows the trend expected from (1.1). The dashed line shows the 2/3 scaling law expected at large scales. The inset graph is a blow-up of the $D_n = 8$ mm data showing that increasing Z_f at constant impact momentum leads to a decrease in H. The data points I–VI correspond to the flow conditions that are compared in § 3.2.

3.2. *Local void fraction measurements*

The aim of this subsection is to present measurements of the local void fraction ϕ within the bubble cloud and discuss them in relation to the bubble cloud size. We discuss first ϕ measurements along the jet axis and then radial profiles of ϕ at a given depth within the cloud. Finally, general remarks on the void fraction profiles are presented.

3.2.1. *Axial measurements*

Figure 3(a) presents the air-to-water volume fraction at the jet axis, $\phi(r = 0, z)$, denoted here by ϕ_0. These measurements correspond to the bubble cloud generated by the $D_n = 2.7$ mm nozzle for two distinct values of jet fall height to diameter ratio Z_f/D_n while maintaining nearly identical impact momentum. The values of ϕ_0 are nearly constant with depth z, until they decrease sharply at the end of the cloud, as reported previously by van de Donk (1981), McKeogh & Ervine (1981), Chanson & Manasseh (2003) and Hoque & Aoki (2008). When Z_f/D_n is increased, a similar axial profile is observed, but ϕ_0 is increased by almost 26 %.

The jet morphology just before impact is illustrated in figure 3(b,c) for $Z_f/D_n = 20$ and 50, and it shows a slightly larger amplitude of the jet undulations for the larger Z_f/D_n case. Using the algorithm introduced in § 2, we measure that the undulations on the jet surface exhibit roughness $\epsilon = 170$ µm for figure 3(b) and $\epsilon = 225$ µm for figure 3(c). As discussed by McKeogh & Ervine (1981) and Sene (1988), we expect the air entrainment rate and therefore the void fraction to be proportional to the volume enclosed by the corrugations observed on the jet surface. The increase in the size of these undulations is therefore certainly what leads to the increase in void fraction observed in figure 3(a). Supplementary movies 1 and 2 (available at https://doi.org/10.1017/jfm.2023. 1019) provide additional visualizations of the jets of figure 3(b,c), respectively (frame rate
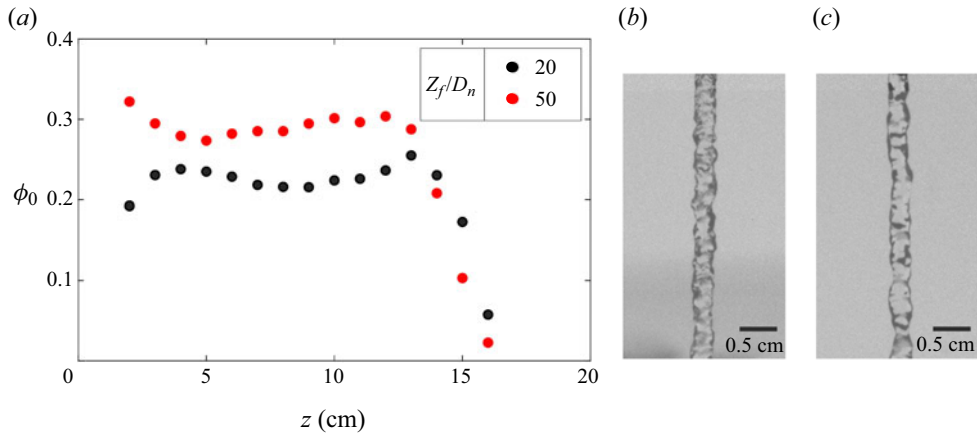
Figure 3. (*a*) Axial evolution of the void fraction $\phi_0(z)$ for two different ratios Z_f/D_n at a fixed jet diameter $D_n = 2.7$ mm and $\sqrt{V_i V_n}\, D_n = 0.016 \pm 0.0002$ m^2 s^{-1}. Instantaneous images of the freely falling jet just before impact: (*b*) $Z_f/D_n = 20$; (*c*) $Z_f/D_n = 50$.

300 images s^{-1}). These two conditions are indicated by labels I and II in figure 2. They are both situated in the inertia-dominated regime, where buoyancy effects are still negligible. As a result, the effect of the void fraction on H is negligible, even though ϕ increases.

3.2.2. *Radial measurements*

Radial profiles of the void fraction are measured for three nozzle diameters, and two heights of fall, at a constant impact momentum. The radial profiles are taken at depths larger than $4D_i$, in order to ensure that they are in the developed region (Ervine & Falvey 1987). Figure 4(*a*) shows the bubble cloud generated by a jet of nozzle diameter $D_n = 2.7$ mm. In comparison, the bubble cloud depth issued from the jet of larger diameter $D_n = 8$ mm, as shown in figure 4(*c*), is significantly smaller (see also labels III and IV in figure 2). The visualizations of figure 4(*a,c*) are illustrated more extensively in supplementary movies 3–6. The void fraction profiles for the 2.7 and 8 mm injectors are shown in figure 4(*b,d*), respectively. They are measured for three different depths. Dispersion in ϕ profiles is relatively small in the developed region. These profiles can be well approximated using a Gaussian distribution (solid lines) as previously reported by van de Donk (1981). This finding is similar to the case where an air jet is injected into the pool (Kobus 1968; Freire *et al.* 2002). When our data are compared with fits based on air/bubble diffusivity and air-to-water volume flux ratio, as in Cummings & Chanson (1997), the best fit was found for an air-to-water entrainment ratio of $\mathcal{O}(10)$! This unrealistic value results perhaps from their constant diffusivity assumption for the advection–diffusion process in the two-phase mixing layer. In our case, and as described by Clanet & Lasheras (1997), the bubbles are convected by the large-scale eddies dominating the evolution of the submerged jet.

Note that the maximum void fraction $\phi(r = 0, z)$ is significantly smaller for the thinner jet (up to 18 % along the axis; see figure 4*b*) than for the larger jet (up to 27 % in figure 4*d*). The impact of the nozzle diameter on the maximum void fraction has already been demonstrated by Chanson *et al.* (2004). The larger void fraction, and hence buoyancy force, is consistent with the observation that the bubble cloud is smaller for the larger diameter. Furthermore, this increase in void fraction is very likely caused by the larger
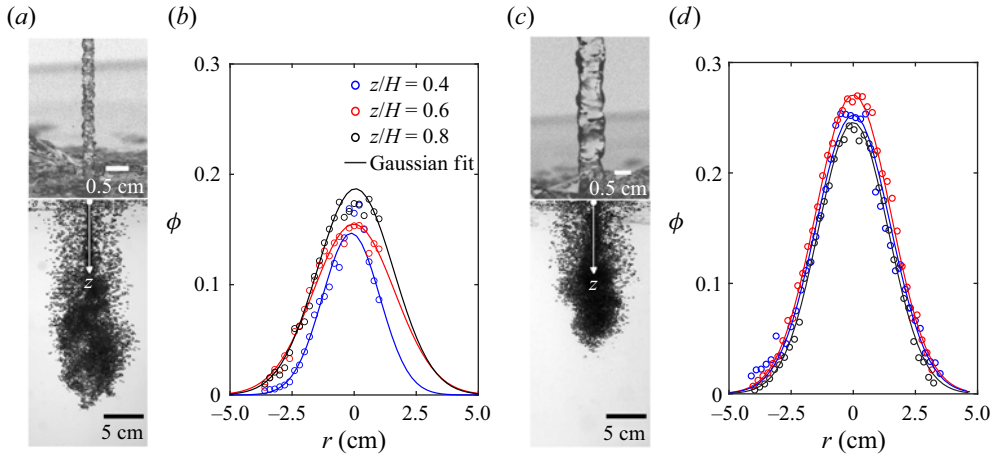
978 A23-8

Figure 4. (*a,c*) Instantaneous pictures of the falling jet just before impact for $D_n = 2.7$ and 8 mm, respectively, at constant $\sqrt{V_i V_n} D_n = 0.028$ m^2 s^{-1} and $Z_f/D_n = 20$. Corresponding bubble clouds are shown as well. (*b,d*) The radial variation of $\phi(r, z)$ at three different depths in the bubble cloud, for the 2.7 mm and 8 mm jets, respectively.

length scales associated with the corrugation and its amplitude occurring on the jet surface when the jet diameter D_n is increased at a constant $Z_f/D_n = 20$ and constant impact momentum (Sene 1988; Liu, Gao & Hu 2022). Measurements of ϵ show that the roughness goes from 225 µm for figure 4(*b*) to 445 µm for figure 4(*d*). These points are indicated by labels III and IV in figure 2. It is clear that III belongs to the momentum-dominated regime, while IV belongs to the buoyancy-dominated regime.

Figure 5 illustrates the influence of a change in the dimensionless jet fall height Z_f/D_n, for a constant impact momentum and constant diameter $D_n = 8$ mm. Photographs of the jet before impact show that the jet issued at $Z_f/D_n = 100$ (figure 5*c*) is more corrugated than that issued at $Z_f/D_n = 20$ (figure 5*a*), for the same $\sqrt{V_i V_n} D_n = 0.075$ m^2 s^{-1}. This is corroborated by the data in figure 6, which show the variation of roughness of the jet at impact (ϵ) and the variation of $\bar{\phi}_0$, the average over depth of the maximum void fraction measured along the axis, as a function of $\sqrt{V_i V_n} D_n$ for different Z_f. The data show a strong increase in ϵ and $\bar{\phi}_0$ as Z_f is increased for a constant momentum. The visualizations of figure 5(*a,c*) are illustrated more extensively in supplementary movies 7–10. The bubble cloud generated below the surface is smaller for the larger Z_f/D_n. Again, this is likely due to the fact that this jet captures more air within its cavities during free-fall, leading to a higher ϕ. This is confirmed by the radial profiles given in figure 5(*b,d*), which show that ϕ_0 for $Z_f/D_n = 100$ is approximately 3.2 times that for $Z_f/D_n = 20$. Note that these cases are referred to by labels V and VI, respectively, in figure 2. They both correspond to the buoyancy-dominated regime. In addition, the inset displayed in figure 2 illustrates a zoomed-in view of the change in H at higher $\sqrt{V_i V_n} D_n$, revealing that an increase in Z_f/D_n results in a reduction of H, with a decrease of approximately 20 % observed when Z_f/D_n is raised from 20 to 100. This ascertains that the observed dispersion for the cloud depth in figure 2 – and also in previous investigations reported in Guyot *et al.* (2020) for this regime, at higher impact momentum and larger diameter – is due to differences in jet fall height.

Finally, general trends of local void fraction profiles are depicted in figure 7 for the case of $D_n = 8$ mm. Each plot presents data at different vertical locations z underneath the surface, normalized with respect to the cloud depth H. In all cases shown here, the data fit
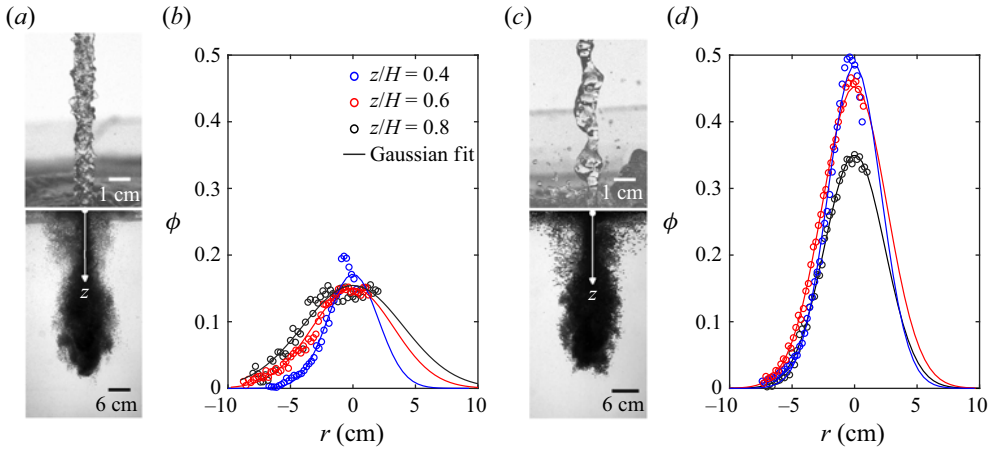
Figure 5. Images of the $D_n = 8$ mm jet just before impact for (a) $Z_f/D_n = 20$ and (c) $Z_f/D_n = 100$, for a constant $\sqrt{V_iV_n}\,D_n = 0.075$ m^2 s^{-1}. Corresponding bubble clouds are shown as well. (b,d) The radial variation of ϕ at various depths in the bubble clouds for $Z_f/D_n = 20$ and 100, respectively.
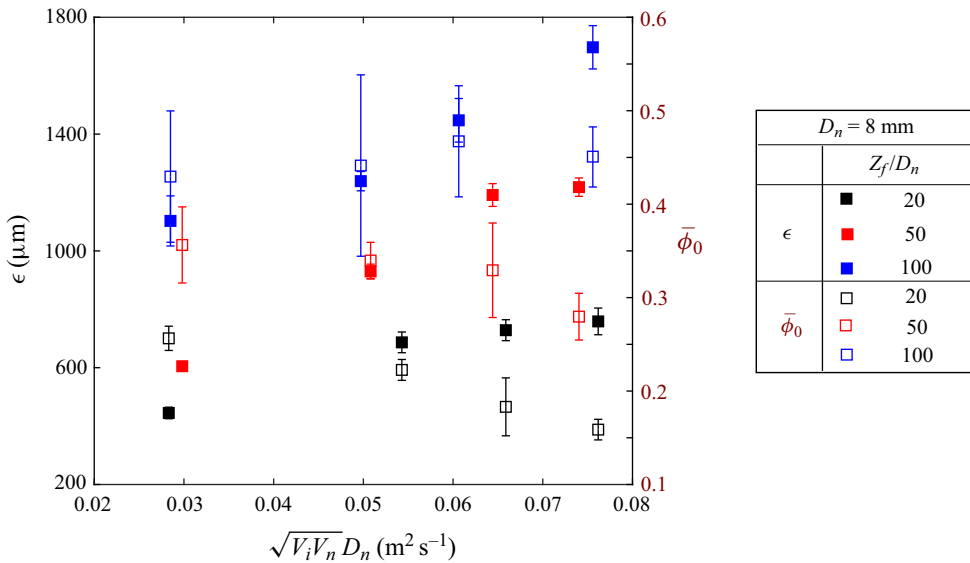

Figure 6. Variation of ϵ and $\bar{\phi}_0$ with $\sqrt{V_iV_n}\,D_n$ for $D_n = 8$ mm, where $\bar{\phi}_0$ is the average over depth of the maximum void fraction measured along the axis. Both ϵ and $\bar{\phi}_0$ increase when Z_f is increased for a constant jet momentum.

reasonably well with a Gaussian profile $\phi = \phi_0(z)\,e^{-r^2/\sigma^2(z)}$ whose peak and width do not vary much as z/H is changed. Plots in figure 7(a) correspond to data for the shortest jet fall height to diameter ratio $Z_f/D_n = 20$ at various $\sqrt{V_iV_n}\,D_n$, a measure of the jet impact momentum up to a factor of liquid density. As $\sqrt{V_iV_n}\,D_n$ increases, the centreline peak void fraction ϕ_0 slightly decreases, while the width of the best-fitting Gaussian profiles increases. On the other hand, at a given $\sqrt{V_iV_n}\,D_n$, the peak void fraction ϕ_0 is almost doubled when the jet's fall height is quintupled. In the next subsection, these observations
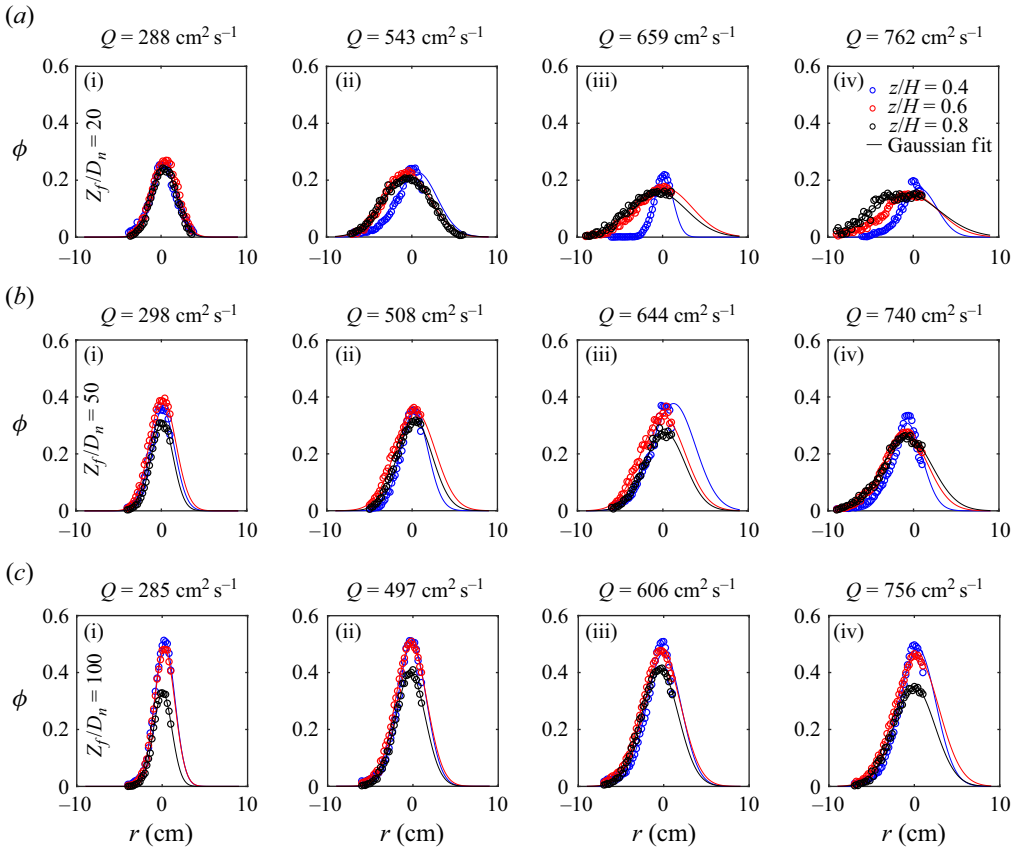
978 A23-10

Figure 7. Measured profiles of air/water void fraction for the nozzle diameter $D_n = 8$ mm and different fall heights (*a*) $Z_f/D_n = 20$, (*b*) $Z_f/D_n = 50$ and (*c*) $Z_f/D_n = 100$, at various values of $Q = \sqrt{V_i V_n} D_n$. Gaussian fits are represented by continuous lines.

on the air-to-water volume fraction in the biphasic region are developed further to capture properly the effect of buoyancy on the bubble cloud depth.

3.3. *Prediction of bubble cloud depth*

Guyot *et al.* (2020) proposed a prediction for the bubble cloud depth H via (1.2) by assuming a uniform void fraction within the bubble cloud and a constant cone angle γ, based on single-phase turbulent jets. As mentioned earlier, the void fraction in the biphasic jet underneath the free surface can be well approximated by a Gaussian profile. These profiles are characterized by a maximum void fraction $\phi_0(z)$ on the axis and a variance $\sigma(z)$. It is then easy to show that the buoyancy force on a slice of bubble cloud of thickness dz at depth z is $dF_b = \phi_0(z) \rho g \pi \sigma(z)^2 dz$. We take $\phi_0(z)$ to be equal to its average value $\bar{\phi}_0$, since the peak void fraction $\phi_0(z)$ exhibits little variation with depth z, as already shown in figures 3–5. It now remains to provide $\sigma(z)$ in order to integrate this buoyancy force over z.

Indeed, it is expected that $\sigma(z)$ increases linearly with depth as the bubble cloud widens up as a cone, as evidenced by visualization and previous observations (Suciu & Smigelschi 1976; McKeogh & Ervine 1981; Clanet & Lasheras 1997; Guyot *et al.* 2020).
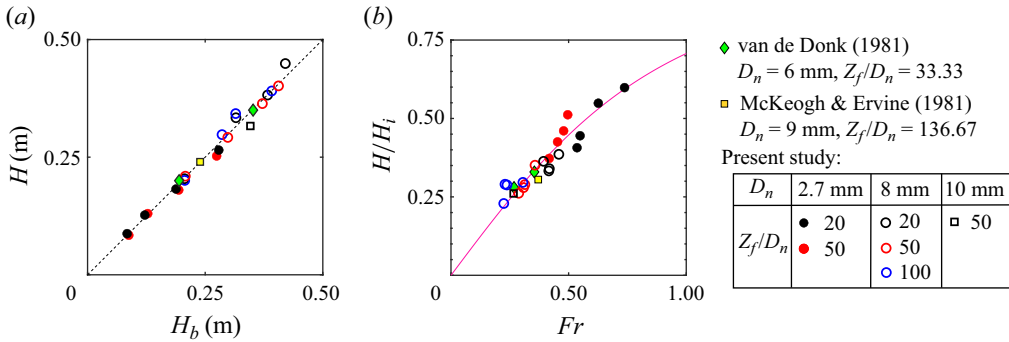
Figure 8. (*a*) Comparison of the experimental depth H with values predicted by the model H_b. (*b*) Normalized depth H/H_i at various values of Fr for injectors from current and past studies whose void fraction is known. Equation (3.2) is represented by the continuous line.

We propose to measure the angle of this cone based on the experimental void fraction profiles. However, rising bubbles can be detected outside the conical jet region by the optical probe. This may lead to overestimation of the width of the void fraction profiles and hence the resulting buoyancy force on the bubble cloud. This is particularly true for the measurements at shallower depths, $z < 0.5H$, a problem also encountered by van de Donk (1981). In order to circumvent this difficulty, the conical jet hypothesis is maintained in accordance with previous authors so that $\sigma(z) = D_i/2 + z \tan \gamma_0$, where the cone angle γ_0 is computed as $\tan \gamma_0 = (\sigma(\tilde{z}) - D_i/2)/\tilde{z}$ at a chosen reference depth $\tilde{z} = 0.8H$. The latter depth was chosen to avoid both rising bubbles and the steep decrease in bubble void fraction in the neighbourhood of the cloud's tail at $z = H$.

Thereby, the net buoyancy force F_b on the bubble cloud of depth H_b can then be expressed as

$$F_b = \bar{\phi}_0 \rho g \pi \left(\frac{1}{3} H_b^3 \tan^2 \gamma_0 + \frac{D_i}{2} H_b^2 \tan \gamma_0 + \frac{D_i^2}{4} H_b \right), \tag{3.1}$$

which is identical to the volume term in (1.2) if $\bar{\phi} = \bar{\phi}_0$ and $\gamma = \gamma_0$. The above expression indicates that the buoyancy force on a conical biphasic jet exhibiting a Gaussian void fraction profile can be interpreted as the buoyancy force exerted on an equivalent biphasic jet with a constant void fraction $\bar{\phi}$ equal to the maximum void fraction $\bar{\phi}_0$ of the Gaussian profile and with a width defined by the variance of the Gaussian profile at some reference depth, here chosen at $z = 0.8H$. This buoyancy force F_b can now be injected into the momentum balance equation (1.2) in order to solve for H_b. The value of $\bar{\phi}$ in the outgoing momentum term can be taken equal to $\bar{\phi}_0$ for the sake of simplicity.

Experimental depths H from the present study and predictions H_b are compared in figure 8(*a*) for the different nozzle sizes and jet fall heights. Good agreement is found between the model and measurements for both the inertia-controlled bubble clouds ($D_n = 2.7$ mm) and the buoyancy-controlled ($D_n = 8$ mm and 10 mm) ones. A measurement for nozzle diameter $D_n = 10$ mm (same length-to-diameter ratio 50), $V_n = 5.5$ m s^{-1} and $Z_f/D_n = 50$ has been included in the data for this figure. For comparison, two previous investigations, namely, those conducted by van de Donk (1981) and McKeogh & Ervine (1981), are presented in figure 8(*a*) as well. They provided both H measurements and radial profiles of ϕ for jets with diameters of $D_n = 6$ and 9 mm. The calculated H_b values based on their measurements show very good consistency with the model.

In what follows, the question of the role of the void fraction in the transition from the inertia-dominated to the buoyancy-dominated regime is discussed. This transition is expected to be dominated by the ratio of the outgoing momentum to the buoyancy force, respectively the second and third terms in (1.2). The square root of the ratio of these terms defines a dimensionless grouping similar to a Froude number, given by $Fr = \sqrt{3(1 - \bar{\phi}_0)/\bar{\phi}_0}\, U_t/\sqrt{gH_b}$. In fact, when the nozzle diameter is small relative to the cloud width $2H_b \tan \gamma_0$, the cubic polynomial for H_b in (1.2) can be rewritten in terms of Fr as

$$\frac{H_b}{H_i} = \frac{Fr}{\sqrt{1 + Fr^2}} + \mathcal{O}\left(\frac{D_i}{2H_b \tan \gamma_0}\, Fr^2\right), \tag{3.2}$$

where H_i is the cloud depth when the buoyancy force is absent, as given by (1.1). When Fr is large, we expect the cloud to be in the inertia-dominated regime and hence H_b to be close to H_i, the simple prediction by Clanet & Lasheras (1997). When, on the contrary, Fr is small, H is expected to be controlled by buoyancy and hence to be significantly smaller than H_i. Figure 8(*b*) illustrates the variation of H/H_i with Fr for data from figure 8(*a*). Indeed, all experimental data points fall on a single curve given by (3.2), for which H/H_i falls steeply when Fr is decreased. For a constant velocity, using larger nozzles will lead to bigger bubble clouds, thus larger H and smaller Fr, thereby favouring the buoyancy-dominated regime. Note also that the influence of jet velocity is counterintuitive here, since a larger jet velocity for a given nozzle diameter will generate a larger H and therefore also favour the buoyancy-dominated regime, instead of the inertial regime. This is because the relevant velocity scale in Fr is the terminal bubble velocity U_t, which is a constant, and not the jet impact velocity. Note that (3.2) is obtained from (1.2) by assuming $\bar{\phi} = \bar{\phi}_0$ and $\gamma = \gamma_0$. This choice simplifies the expression of the Froude number, but obviously underestimates the jet angle and mean void fraction in the inertial contribution. This is partly the reason why H/H_i does not reach the limit $H/H_i = 1$ in figure 8(*b*), even for data points that corresponded to the inertia-dominated regime in figure 2. Furthermore, previous authors have proposed adding a hemispherical dome to the truncated cone modelling the bubble cloud, as in figure 1 (Clanet & Lasheras 1997; Guyot *et al.* 2020). This small correction would introduce a factor of $1 + \tan \gamma_0$ (of the order of 10 %) to both the modelled heights H_i and H_b, but it is not considered in the present data for the sake of simplicity.

For most studies for which bubble cloud depths data are available, the void fraction has not been measured concomitantly. We plot in figure 9(*a*) H as a function of $\sqrt{V_i V_n}\, D_n$, the square root of the impact momentum over the liquid density ρ, for five past studies covering a wide range of scales, plus the present data. The scaling laws observed in figure 2 for the inertia-dominated and buoyancy-dominated regimes can be observed in the limits of low momentum and large momentum, respectively. The void fraction is not known for these past works, but we can still estimate the bubble cloud Froude number as $Fr^* = U_t/\sqrt{gH}$. Figure 9(*b*) shows that when H/H_i is plotted as a function of Fr^* for several past studies, the cloud sizes are clearly sorted into two regimes: (i) one for larger $Fr^* > 0.2$, for which H/H_i is close to 1 and for which there is little dispersion; and (ii) a second regime for $Fr^* < 0.2$ where H/H_i varies between 0.15 and 0.5, and for which significant dispersion is obtained. This dispersion is very likely due to the role of the void fraction, which has been omitted in Fr^*. These observations ascertain further that Fr is a good parameter for monitoring the transition between the inertia-dominated and buoyancy-dominated regimes.
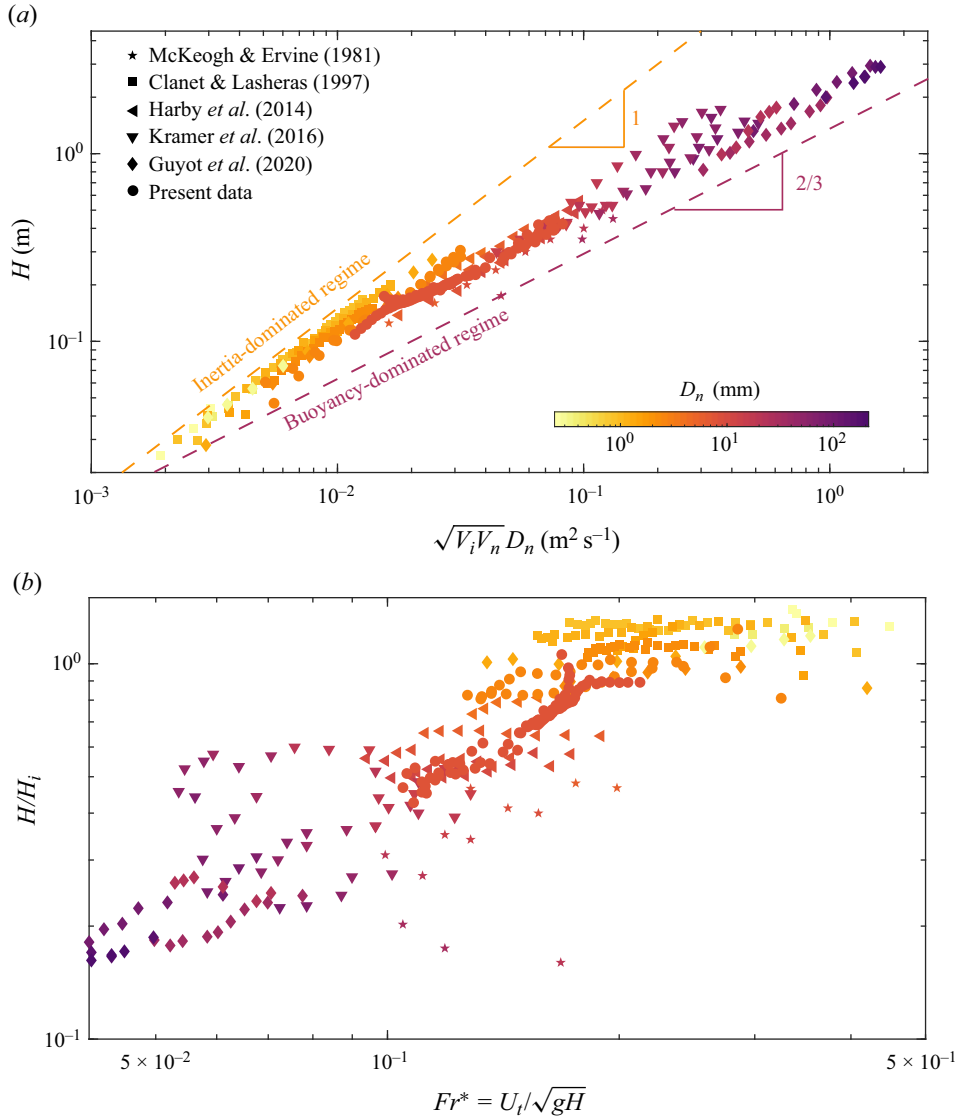
Figure 9. (*a*) Bubble cloud depth (H) data from previous investigations are presented here as a function of $\sqrt{V_i V_n} D_n$, a measure of the impact momentum, to illustrate the two distinct dynamical regimes identified in our study over a wide range of scales. (*b*) When the void fraction is not known, Fr^* can still sort past experiments into inertia- or buoyancy-dominated regimes, even though more dispersion is observed.

3.4. *Equivalent bubble cloud void fraction* ϕ_b

Whereas Guyot *et al.* (2020) took a uniform void fraction within the cloud to express the momentum balance, ϕ profiles were observed here to follow a Gaussian distribution in the radial direction. In this subsection, an equivalent constant void fraction ϕ_b is proposed in order to provide a bulk quantity for a bubble cloud and to discuss its variations with the jet fall height and impact momentum. At first, for a fixed depth z, the edge of this constant-void-fraction cone of bubble cloud is defined by assuming that its radius $R_b(z)$, beyond which the void fraction becomes zero, is the radius at
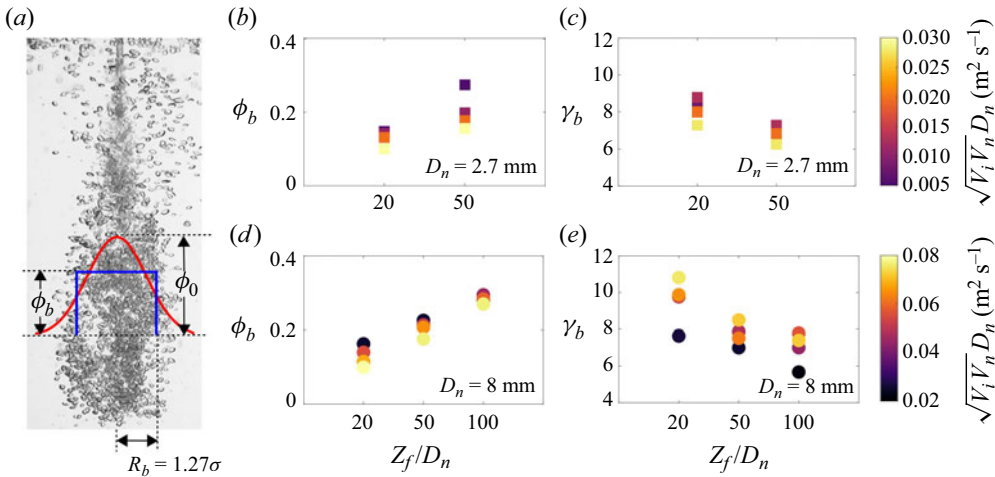
Figure 10. (*a*) Definition of ϕ_b and R_b. (*b–e*) Variation of ϕ_b and γ_b with Z_f/D_n for the two injector sizes at various impact momentum values. Two colour bars are provided for the two ranges of $\sqrt{V_i V_n}\, D_n$, corresponding to both D_n values.

which 80 % of the surface-integrated void fraction is attained based on a Gaussian profile $\phi = \bar{\phi}_0(z)\, e^{-r^2/\sigma(z)^2}$. This simply gives the relation $R_b(z) = \sigma(z)\sqrt{\log 5} \approx 1.27\sigma$. Thereafter, in order to avoid overestimation of the bubble cloud volume due to rising bubbles, the truncated cone angle γ_b for this constant-void-fraction cloud is taken as $\tan\gamma_b = (\tilde{R}_b - D_i/2)/\tilde{z}$, where $\tilde{R}_b \approx 1.27\,\sigma(\tilde{z})$ is this cloud's radius at the reference depth $\tilde{z} = 0.8H$. As already mentioned in § 3.3, the influence of rising bubbles is minimal at the reference depth $\tilde{z} = 0.8H$, measured close to the bottom of the cloud, while the peak void fraction ϕ_0 is still comparable to those obtained in the bulk. Finally, the equivalent void fraction ϕ_b is then computed such that the net buoyancy force is the same on both the uniform-void-fraction cloud and the Gaussian-void-fraction cloud.

Figure 10(*b,d*) depict the evolution of this equivalent void fraction ϕ_b as a function of Z_f/D_n, for different values of impact momentum (represented by the colour) for the two injectors. Experimental results show that ϕ_b increases steeply for both injectors as Z_f/D_n increases, as already illustrated in figure 5 for a particular case. As mentioned in § 3.2.2, this is likely due to the jet's capacity to entrain more air once perturbations have grown larger on its surface for higher fall heights Z_f (Sene 1988). These plots also show that ϕ_b decreases for a constant Z_f/D_n as the impact momentum is increased, in particular for low Z_f/D_n.

Figure 10(*c,e*) illustrate the variations of the cone angle γ_b of the equivalent constant-ϕ jet with respect to Z_f/D_n, for different $\sqrt{V_i V_n}\, D_n$. Results for both nozzles show that γ_b decreases with Z_f/D_n for a constant impact momentum. This change in the bubble cloud shape may be related to the strong increase in the amplitude of surface perturbations at larger Z_f, and to the larger void fractions observed for these conditions (ϕ_0 up to 50 % for $Z_f/D_n = 100$, compared with 20 % for $Z_f/D_n = 20$). The simple assumptions made regarding the shape of the bubble cloud, which are valid at moderate void fractions, probably no longer hold in such conditions.

978 A23-15

4. Conclusion

Experiments on circular plunging jets have been carried out to characterize the two regimes for bubble cloud formation, namely the inertia-dominated and buoyancy-dominated regimes. Void fraction profiles were measured in the developed region of the cloud with novel optical probes for nozzle diameters $D_n = 2.7$, 8 and 10 mm. They can be well approximated by Gaussian distributions. When these measurements are incorporated into the momentum balance model, taking into account only the buoyancy force, the model predicts the experiments very well for both current and past studies. Even though the void fraction measurements have been carried out only for nozzle sizes smaller than 1 cm and bubble cloud sizes smaller than 50 cm, it is expected that this result still holds at larger scales, as already proposed by Guyot *et al.* (2020). This will have to be verified with void fraction measurements in such metric scale systems in future works.

The threshold between the inertia and buoyancy regimes is shown to be dependent on a characteristic Froude number *Fr* composed of the terminal bubble velocity U_t, the cloud depth H and the void fraction within the bubble cloud. For large values of this number, H can be estimated with the simple model of Clanet & Lasheras (1997), while for low values of *Fr* it is buoyancy that controls the bubble cloud size. The fact that a single equation can predict bubble cloud size independent of scale and of the wide zoology of jet dynamics, provided that the void fraction is known, is the major result of this work.

A constant equivalent void fraction ϕ_b is also introduced based on the integration of the Gaussian void fraction profiles. The variations of ϕ_b and of the corresponding jet cone angle γ_b with the impact momentum and the jet fall height to diameter ratio Z_f/D_n are discussed. This void fraction ϕ_b is expected to be a function of the jet diameter, height of fall and velocity (Wang *et al.* 2018). Data show that an increase in the height of fall Z_f leads to a significant increase in the void fraction within the cloud, which in turn leads to a decrease in the bubble cloud size. The modelling of ϕ_b as a function of jet dynamics, which is necessary for practical purposes if one wishes to predict H solely as a function of input parameters, is a question that future works will have to address.

Author ORCIDs.
- Narendra Dev https://orcid.org/0009-0007-4626-3585;
- J. John Soundar Jerome https://orcid.org/0000-0003-2148-9434;
- Hélène Scolan https://orcid.org/0000-0003-2739-2297;
- Jean-Philippe Matas https://orcid.org/0000-0003-0708-1619.

REFERENCES

BERTOLA, N., WANG, H. & CHANSON, H. 2018 A physical study of air–water flow in planar plunging water jet with large inflow distance. *Intl J. Multiphase Flow* **100**, 155–171.

BIŃ, A.K. 1993 Gas entrainment by plunging liquid jets. *Chem. Engng Sci.* **48** (21), 3585–3630.

BONETTO, F., DREW, D. & LAHEY, R.T. JR. 1994 The analysis of a plunging liquid jet – the air entrainment process. *Chem. Engng Commun.* **130** (1), 11–29.

BONETTO, F. & LAHEY, R.T. 1993 An experimental study on air carryunder due to a plunging liquid jet. *Intl J. Multiphase Flow* **19** (2), 281–294.

BRATTBERG, T. & CHANSON, H. 1998 Air entrapment and air bubble dispersion at two-dimensional plunging water jets. *Chem. Engng Sci.* **53** (24), 4113–4127.

CHANSON, H. 2002 *Hydraulics of Stepped Chutes and Spillways*. CRC Press.

CHANSON, H., AOKI, S. & HOQUE, A. 2004 Physical modelling and similitude of air bubble entrainment at vertical circular plunging jets. *Chem. Engng Sci.* **59** (4), 747–758.

CHANSON, H. & MANASSEH, R. 2003 Air entrainment processes in a circular plunging jet: void-fraction and acoustic measurements. *Trans. ASME J. Fluids Engng* **125** (5), 910–921.

CHIRICHELLA, D., GOMEZ LEDESMA, R., KIGER, K.T. & DUNCAN, J.H. 2002 Incipient air entrainment in a translating axisymmetric plunging laminar jet. *Phys. Fluids* **14** (2), 781–790.

CLANET, C. & LASHERAS, J.C. 1997 Depth of penetration of bubbles entrained by a plunging water jet. *Phys. Fluids* **9** (7), 1864–1866.

CUMMINGS, P.D. & CHANSON, H. 1997 Air entrainment in the developing flow region of plunging jets – part 1: theoretical development. *Trans. ASME J. Fluids Engng* **119** (3), 597–602.

CUMMINGS, P.D. & CHANSON, H. 1999 An experimental study of individual air bubble entrainment at a planar plunging jet. *Chem. Engng Res. Des.* **77** (2), 159–164.

VAN DE DONK, J.A.C. 1981 Water aeration with plunging jets. PhD thesis, Delft University of Technology, Delft, The Netherlands.

EL HAMMOUMI, M., ACHARD, J.-L. & DAVOUST, L. 2002 Measurements of air entrainment by vertical plunging liquid jets. *Exp. Fluids* **32**, 624–638.

ERVINE, D.A. & FALVEY, H.T. 1987 Behaviour of turbulent water jets in the atmosphere and in plunge pools. *Proc. Inst. Civ. Engrs* **83** (1), 295–314.

FREIRE, A.P.S., MIRANDA, D.D.E., LUZ, L.M.S. & FRANÇA, G.F.M. 2002 Bubble plumes and the Coanda effect. *Intl J. Multiphase Flow* **28** (8), 1293–1310.

GUYOT, G. 2019 Contribution à la caractérisation des processus d'entraînement d'air dans les circuits d'aménagements hydro-électriques. PhD thesis, Université Grenoble Alpes, France.

GUYOT, G., CARTELLIER, A. & MATAS, J.-P. 2019 Depth of penetration of bubbles entrained by an oscillated plunging water jet. *Chem. Engng Sci.* **2**, 100017.

GUYOT, G., CARTELLIER, A. & MATAS, J.-P. 2020 Penetration depth of a plunging jet: from microjets to cascades. *Phys. Rev. Lett.* **124** (19), 194503.

HARBY, K., CHIVA, S. & MUÑOZ-COBO, J.L. 2014 An experimental study on bubble entrainment and flow characteristics of vertical plunging water jets. *Expl Therm. Fluid Sci.* **57**, 207–220.

HOQUE, A. & AOKI, S. 2008 Air entrainment and associated energy dissipation in steady and unsteady plunging jets at free surface. *Appl. Ocean Res.* **30** (1), 37–45.

HORN, G. & THRING, M.W. 1956 Angle of spread of free jets. *Nature* **178** (4526), 205–206.

KAPUR, J.N., SAHOO, P.K. & WONG, A.K.C. 1985 A new method for gray-level picture thresholding using the entropy of the histogram. *Comput. Vis. Graph. Image Process.* **29** (3), 273–285.

KIGER, K.T. & DUNCAN, J.H. 2012 Air-entrainment mechanisms in plunging jets and breaking waves. *Annu. Rev. Fluid Mech.* **44**, 563–596.

KIRILLOV, A., *et al.* 2023 Segment Anything. arXiv:2304.02643.

KOBUS, H.E. 1968 Analysis of the flow induced by air-bubble systems. In *Proc. 11th Conf. Coastal Engineering, London, United Kingdom, September 1968* (ed. M.P. O'Brien), pp. 1016–1031. American Society of Civil Engineers.

KRAMER, M., WIEPRECHT, S. & TERHEIDEN, K. 2016 Penetration depth of plunging liquid jets – a data driven modelling approach. *Expl Therm. Fluid Sci.* **76**, 109–117.

LIN, T.J. & DONNELLY, H.G. 1966 Gas bubble entrainment by plunging laminar liquid jets. *AIChE J.* **12** (3), 563–571.

LIU, C., GAO, R. & HU, C. 2022 A consistent mass–momentum flux computation method for the simulation of plunging jet. *Phys. Fluids* **34** (3), 032114.

LIU, S., *et al.* 2023 Grounding DINO: Marrying DINO with grounded pre-training for open-set object detection. arXiv:2303.05499.

LORENCEAU, É., QUÉRÉ, D. & EGGERS, J. 2004 Air entrainment by a viscous jet plunging into a bath. *Phys. Rev. Lett.* **93** (25), 254501.

L'VOV, V.S., POMYALOV, A., PROCACCIA, I. & GOVINDARAJAN, R. 2008 Random vortex-street model for a self-similar plane turbulent jet. *Phys. Rev. Lett.* **101** (9), 094503.

MA, J., OBERAI, A.A., DREW, D.A., LAHEY, R.T. JR. & Moraga, F.J. 2010 A quantitative sub-grid air entrainment model for bubbly flows – plunging jets. *Comput. Fluids* **39** (1), 77–86.

MAXWORTHY, T., GNANN, C., KÜRTEN, M. & DURST, F. 1996 Experiments on the rise of air bubbles in clean viscous liquids. *J. Fluid Mech.* **321**, 421–441.

MCKEOGH, E.J. & ERVINE, D.A. 1981 Air entrainment rate and diffusion pattern of plunging liquid jets. *Chem. Engng Sci.* **36** (7), 1161–1172.

MIWA, S., MORIBE, T., TSUTSUMI, K. & HIBIKI, T. 2018 Experimental investigation of air entrainment by vertical plunging liquid jet. *Chem. Engng Sci.* **181**, 251–263.

QU, X., GOHARZADEH, A., KHEZZAR, L. & MOLKI, A. 2013 Experimental characterization of air-entrainment in a plunging jet. *Expl Therm. Fluid Sci.* **44**, 51–61.

ROY, A.K., MAITI, B. & DAS, P.K. 2013 Visualisation of air entrainment by a plunging jet. *Procedia Engng* **56**, 468–473.

SCHINDELIN, J., *et al.* 2012 Fiji: an open-source platform for biological-image analysis. *Nat. Meth.* **9** (7), 676–682.

SENE, K.J. 1988 Air entrainment by plunging jets. *Chem. Engng Sci.* **43** (10), 2615–2623.

SPEIRS, N.B., PAN, Z., BELDEN, J. & TRUSCOTT, T.T. 2018 The water entry of multi-droplet streams and jets. *J. Fluid Mech.* **844**, 1084–1111.

SUCIU, G.D. & SMIGELSCHI, O. 1976 Size of the submerged biphasic region in plunging jet systems. *Chem. Engng Sci.* **31**, 1217–1220.

TSAI, W.-H. 1985 Moment-preserving thresholding: a new approach. *Comput. Vis. Graph. Image Process.* **29** (3), 377–393.

VAN DE SANDE, E. & SMITH, J.M. 1973 Surface entrainment of air by high velocity water jets. *Chem. Engng Sci.* **28** (5), 1161–1168.

VAN DE SANDE, E. & SMITH, J.M. 1976 Jet break-up and air entrainment by low velocity turbulent water jets. *Chem. Engng Sci.* **31** (3), 219–224.

WANG, H., SLAMET, N.S., ZHANG, G. & CHANSON, H. 2018 Intrusive measurements of air–water flow properties in highly turbulent supported plunging jets and effects of inflow jet conditions. *Chem. Engng Sci.* **177**, 245–260.

ZHU, Y., OĞUZ, H.N. & PROSPERETTI, A. 2000 On the mechanism of air entrainment by liquid jets at a free surface. *J. Fluid Mech.* **404**, 151–177.